Achieving High Efficiency in Solution-Processed Perovskite Solar Cells using C_{60}/C_{70} Mixed Fullerenes

Hao-Sheng Lin[1], Il Jeon[1]*, Rong Xiang[1], Seungju Seo[1], Jin-Wook Lee[2], Chao Li[2], Amrita Pal[3], Sergei Manzhos[3], Mark S.Goorsky[2], Yang Yang[2], Shigeo Maruyama[1], and Yutaka Matsuo[1,4]*

[1]Department of Mechanical Engineering, The University of Tokyo, 7-3-1 Hongo, Bunkyo-ku, Tokyo 113-8656, Japan

[2]Department of Mechanical Engineering, National University of Singapore, Block EA #07-08, 9 Engineering Drive 1, Singapore 117576, Singapore

[3]Department of Materials Science and Engineering, University of California, Los Angeles, Los Angeles, CA 90095, USA

[4]Hefei National Laboratory for Physical Sciences at the Microscale, University of Science and Technology of China, Hefei, Anhui 230026, China

ABSTRACT

Fullerenes have attracted considerable interest as an electron transporting layer in perovskite solar cells. Fullerene-based perovskite solar cells produce no hysteresis and do not require high-temperature annealing. However, high power conversion efficiency can only be achieved when the fullerene layer is thermally evaporated, which is an expensive process. In this work, the limitations of a solution-processed fullerene layer have been identified as high crystallinity and the presence of remnant solvents, in contrast to a thermally deposited C_{60} film, which has low crystallinity and no remaining solvents. As a solution to these problems, a mixed C_{60} and C_{70} solution-processed film, which exhibits low crystallinity, is proposed as an electron transporting layer. The mixed-fullerene-based devices produce power conversion efficiencies as high as that of the thermally evaporated C_{60}-based device (16.7%), owing to improved fill factor and open-circuit voltage. In addition, by vacuum-drying the mixed fullerene film, the power conversion efficiency of the solution-processed perovskite solar cells is further improved to 18.0%. This improvement originates from the enhanced transmittance and charge transport by removing the solvent effect. This simple and low-cost method can be easily used in any type of solar cells with fullerene as the electron transporting layer.

1. INTRODUCTION

Organometal halide perovskite solar cells (PSCs) have emerged as next-generation thin-film solar energy harvesters with high efficiency, owing to the long exciton diffusion length, high absorption coefficient, and high carrier mobility of the perovskite.[1–5] Fullerenes, which have been used in organic solar cells (OSCs) for more than two decades, have attracted considerable interest as an electron transporting layer (ETL) in PSCs.[6] Unlike in OSCs, fullerenes are not used as an electron acceptor in the photoactive layer of PSCs; instead, fullerenes function as a charge-selective layer in PSCs and high concentration of fullerene solution is not necessary for PSCs. Furthermore, pristine fullerenes, such as [60]fullerene (C_{60}) and [70]fullerene (C_{70}), which possess intrinsically higher mobility and conductivity than fullerene derivatives, can be directly applied to PSCs without difficult and expensive chemical modification.[7–10] Currently, metal oxides ETLs, such as TiO_2 and SnO_2, are widely used in PSCs. However, the use of metal oxide ETLs results in large hysteresis of devices,[11] originating from charge accumulation[12] and charge trapping[13,14]. Moreover, their high sintering temperature limits the flexible and large-size application of PSCs[15,16]. Fullerenes can be used as an ETL to avoid these problems.[17,18] Fullerenes have low chemical capacitance and high electron affinity, which helps avoid hysteresis.[19,20] In addition, fullerenes are reported to function as a passivation layer for perovskite grain boundaries, reducing the surface trap density.[21,22] Nevertheless, high power conversion efficiencies (PCEs) were reported only when fullerenes were thermally deposited or over-coated on metal oxides; the thermal deposition is a slow and expensive process, and the over-coating process requires a metal oxide layer, which renders the use of fullerenes futile.[23–25] Spin coating of fullerene solution, which is a simple and low-cost process that enables large-size

application, is an ideal alternative. However, solution-processed (spin-coated) fullerene-based PSCs cannot achieve PCEs as high as those of thermally deposited fullerene-based PSCs.

In this work, we studied the reasons for the lower performance of spin-coated fullerene-based PSCs compared with that of thermally deposited fullerene PSCs. Accordingly, we provide a method for achieving higher efficiency using spin-coated fullerenes. With regard to pristine fullerenes, we compared thermally deposited and spin-coated pristine fullerenes in PSCs, and observed that C_{60} is a better ETL than C_{70}, owing to its lower absorption and better morphology. In addition, thermally deposited fullerenes are a better ETL than spin-coated fullerenes, owing to the amorphous state of the thermally deposited C_{60} films in contrast to the crystalline state of the spin-coated C_{60} films. Considering that the crystallinity of the fullerene films is linked to the performance of ETLs, we showed that mixing C_{70} into C_{60} reduces the crystallinity of the film. Consequently, the spin-coated mixed-fullerene-based PSC devices produced a PCE of 16.7%, which is similar to that of thermally deposited C_{60}-based PSCs. To enhance the performance of the spin-coated mixed-fullerene-based PSCs further, the fullerene films were subjected to vacuum drying to remove the remaining solvents. The removal of the intercalated solvent from the fullerenes improved the optical transparency and charge transport of the film. The vacuum-dried spin-coated mixed-fullerene-based PSCs produced a PCE of 18.0%, which was significantly higher than that of the thermally evaporated fullerene-based PSCs. This study not only achieved a high PCE of the spin-coated fullerene-based PSCs, but also provided an insight into the fullerene engineering of PSCs through various analyses.

2. RESULTS AND DISCUSSION

2.1. Investigation of Pristine Fullerene ETLs in PSCs.

There have been a few reports on the comparison between C_{60} and C_{70} as the ETL in PSCs, but these comparisons were limited in terms of device architectures and deposition methods.[23,26,27] Some of these reports contradicted each other in terms of PCEs and analyses. Therefore, we first comprehensively compare C_{60} and C_{70} in normal and inverted architectures using thermal and solution deposition methods **(Figure 1a and S1)**. **Table 1** shows the photovoltaic performance of the thermally deposited C_{60}- and C_{70}-based PSCs in the normal and inverted architectures **(Figure S2)**. In both device types, the C_{60}-based PSCs produced higher PCEs than the C_{70}-based devices, which is consistent with the previous reports.[23,26,27] The same open-circuit voltage (V_{OC}) values of the C_{60}- and C_{70}-based devices indicate that C_{60} and C_{70} possess similar energy disorders[28–30] and similar energy levels, which are supported by the ab initio calculations **(Figure 1b, Figure S3)** and photoelectron yield spectroscopy (PYS) measurements **(Figure S4)**.[31,32] The density functional theory (DFT) calculations of C_{60} and C_{70} single molecules reveal that they have similar lowest unoccupied molecular orbital (LUMO) levels whereas their highest occupied molecular orbital levels are within 0.1 eV of each other **(Figure S3)**. This result is corroborated by PYS data, which show that the valence levels of C_{60} and C_{70} are -6.4 eV and -6.3 eV, respectively, for both thermally deposited and spin-coated films **(Figure S4a, b, c, and d)**. The short-circuit current density (J_{SC}) was lower for the C_{70}-based PSCs than for the C_{60}-based PSCs for the normal architecture, but was similar for both PSCs for the inverted architecture. This indicates that the lower J_{SC} is due to the higher absorption of C_{70} **(Figure S5 and S6)**. The fill factor (FF) of the C_{70}-based PSCs was lower than that of the C_{60}-based PSCs for both the normal- and inverted-type devices. The lower FF of the C_{70}-based PSCs is due to the higher series resistance (R_S) and lower shunt resistance (R_{SH}). Previous studies reported that C_{70} thin-films have higher conductivity[33,34] and electron affinity[35] than C_{60} thin-films. Moreover, C_{70} is

observed to be more effective in preventing the recombination of excitons than C_{60}, because C_{60} possesses many circulating circuits, resulting in inefficient quantum current distributions inside the molecules.[36] However, based on photoluminescence (PL) measurement (**Figure 1c**), it was observed that the C_{60} films quenched the excitons from $MAPbI_3$ better than the C_{70} films. Notably, the PL peak of $MAPbI_3$ on C_{60} films is blue-shifted slightly. This blue shift indicates the passivation of the trap states between C_{60} and $MAPbI_3$ as the trap states lead to spontaneous radiative recombination at the surface.[21] Furthermore, the full width at half maximum (FWHM) was narrower for the $MAPbI_3$ on C_{60} compared with that on C_{70}. The narrower FWHM indicates a reduction in the shallow trap density at the interface.[37] It has been reported that the low molecular symmetry of C_{70} leads smoother morphology of C_{60} leads to better electron transfer from $MAPbI_3$.[38,39] Therefore, we can conclude that the higher FF is due to the better interface between C_{60} and $MAPbI_3$, thus facilitating the use of C_{60} as the ETL in PSCs.
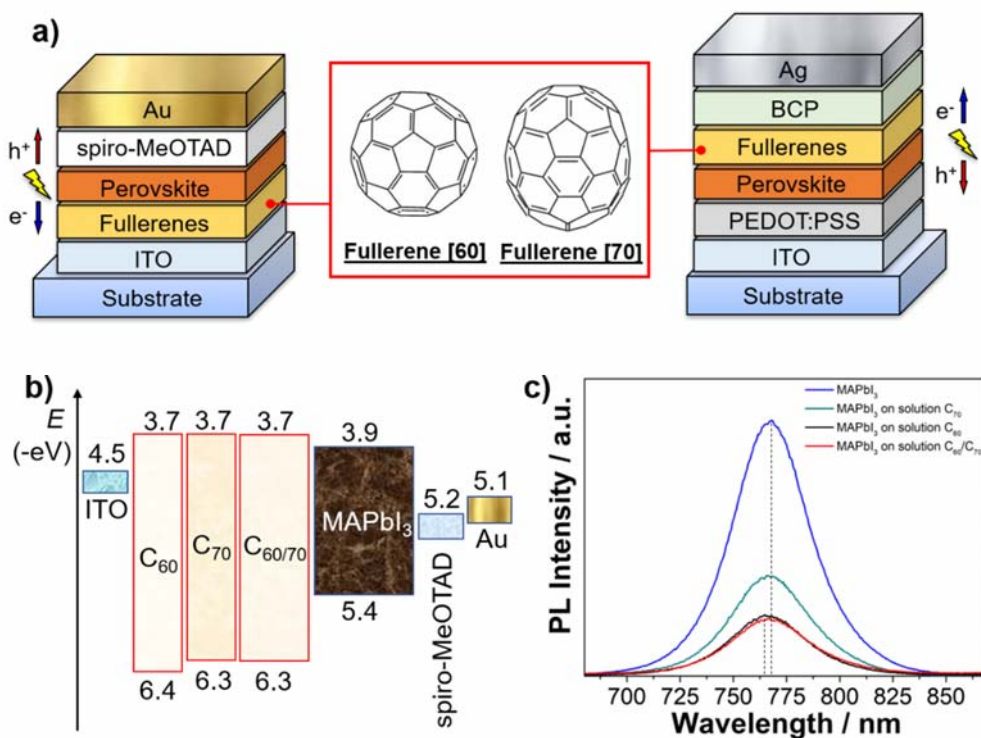

Figure 1. a) Illustration of normal-type and inverted-type PSC structures used in this work with C_{60} and C_{70} molecules. b) Calculated energy band diagrams of C_{60}, C_{70}, and mixed fullerene

analyses in a normal-type PSC. c) Photoluminescence of MAPbI$_3$ on glass (blue line), MAPbI$_3$ on C$_{70}$ on glass (green line), MAPbI$_3$ on C$_{60}$ on glass (black line), and MAPbI$_3$ on C$_{60}$/C$_{70}$ on glass (red line).

Table 1. Photovoltaic parameters of the normal-type and inverted-type PSCs using thermally evaporated C$_{60}$ and C$_{70}$ as the ETLs under one sun (AM 1.5 G, 100 mW cm^{-2}).

Device Type	Fullerene	J_{SC} [mA cm^{-2}]	V_{OC} [V]	FF	R_S [Ω cm^2]	R_{SH} [Ω cm^2]	PCE$_{Best}$	PCE$_{Average}$	Hysteresis Index[11b]
Normal	C$_{60}$	22.7	1.01	0.72	37	3.7×10^4	16.7%	16.6% ±0.4	0.01
	C$_{70}$	19.3	1.01	0.63	41	2.3×10^4	12.3%	12.1% ±0.2	0.03
Inverted	C$_{60}$	22.9	0.90	0.77	9	1.1×10^4	15.8%	15.3% ±0.4	0.01
	C$_{70}$	22.9	0.91	0.55	27	7.2×10^3	11.4%	11.3% ±0.3	0.02

Spin-coated C$_{60}$ and C$_{70}$ films were compared in the normal-type PSCs. As the normal-type PSCs exhibit higher efficiency than the inverted-type PSCs, we only consider the normal architecture henceforth. The difference between the spin-coated C$_{60}$- and C$_{70}$-based PSCs was similar to that between the thermally deposited C$_{60}$- and C$_{70}$-based PSCs (**Table 2, Figure S7a**); the C$_{70}$-based devices showed a lower J_{SC} and FF than the C$_{60}$-based devices. Spin-coated fullerene-based PSCs showed lower PCEs than the thermally deposited fullerene-based PSCs (based on a comparison between **Table 1** and **Table 2**). Although the spin-coated fullerene-based PSCs resulted in lower efficiency, the solution process is preferred over the thermal deposition process owing to its lower fabrication cost, higher speed, and simplicity. Thus, it is important to determine why the spin-coated fullerene-based devices resulted in lower performance than the thermal-processed PSCs and to provide a solution to this limitation.

As the lower V_{OC} and FF resulted in the lower PCE of the spin-coated fullerene-based PSCs (thermally deposited C_{60}-based PSCs: J_{SC} = 22.7 mA cm^{-2}, V_{OC} = 1.01 V, FF = 0.72 from **Table 1**; spin-coated C_{60}-based PSCs: J_{SC} = 23.0 mA cm^{-2}, V_{OC} = 0.99 V, FF = 0.65 from **Table 2**), we attribute the lower performance mainly to the crystallinity of fullerene films. In general, thermally deposited fullerene films are reported to be nearly amorphous,[40–42] whereas spin-coated fullerene films are reported to possess high crystallinity.[42–45] We used grazing-incidence X-ray diffraction spectroscopy (GIXRD) to analyze the thermally evaporated C_{60} films and the spin-coated C_{60} films (**Figure S8**). **Figure 2a** shows that the spectra of the thermally deposited C_{60} films do not display any peaks, but those of the spin-coated C_{60} films display the (111) peak at 10° and the (220) peak at 18°.[46] This was also confirmed by the transmission electron microscope (TEM) images. The thermally deposited C_{60} films exhibited an amorphous state (**Figure 2b, Figure S9a**) with no crystal domains (**Figure 2c**), whereas the spin-coated C_{60} films exhibited high crystallinity (**Figure 2d, Figure S9b**) with crystal domains of sizes 20 nm to 100 nm (**Figure 2e, Figure S9c**). It is known that the boundaries between crystal domains hinder the charge flow whereas charge mobility may be high within a crystal domain. Therefore, unless a film is in a predominately single crystalline phase, amorphous films are expected to have better charge transport. This explains the higher series resistance (R_S) and lower FF of the spin-coated C_{60}-based PSCs as compared with those of the thermally deposited C_{60}-based PSCs. The lower charge transport indicates more charge recombination; thus, lower V_{OC} was obtained for the spin-coated fullerene-based PSCs.
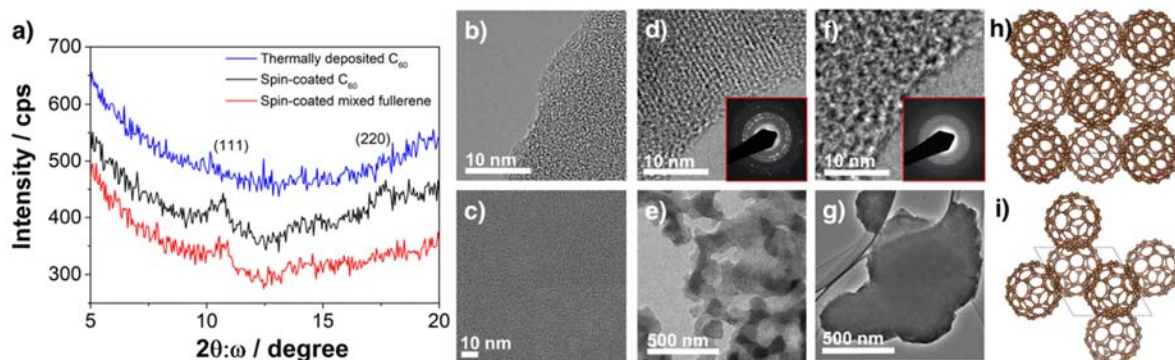
Figure 2. a) GIXRD 2θ scan (incident angle ω = 1 degree) of thermally deposited C_{60} film (blue line), spin-coated C_{60} film (black line), and spin-coated mixed fullerene film (red line). TEM images of b), c) thermally deposited C_{60} film; d), e) spin-coated C_{60} film with an SAED as an inset; and f), g) spin-coated mixed fullerene film with an SAED as an inset. Optimized structures using Grimme dispersion parameters of h) C_{60} in fcc crystal structure, and i) C_{70} in hcp crystal structure.

Table 2. Photovoltaic parameters of the normal-type PSCs using spin-coated C_{60}, C_{70}, and mixed fullerene with different ratio as the ETLs under one sun (AM 1.5 G, 100 mW cm^{-2}).

Fullerene	J_{SC} [mA cm^{-2}]	V_{OC} [V]	FF	R_S [Ω cm^2]	R_{SH} [Ω cm^2]	PCE_{Best}	$PCE_{Average}$	Hysteresis Index
C_{60}	23.0	0.99	0.65	42	1.7×10^4	14.8%	14.6% ±0.7	0.03
C_{70}	19.5	0.97	0.62	36	6.8×10^4	11.7%	11.4% ±0.6	0.07
C_{60}/C_{70} (9:1)	22.9	1.02	0.71	30	1.5×10^5	16.7%	16.6% ±0.5	0.04
C_{60}/C_{70} (5:5)	21.2	1.02	0.55	65	5.7×10^3	11.8%	11.4% ±0.5	0.05
C_{60}/C_{70} (1:9)	20.4	1.00	0.55	60	6.8×10^3	11.1%	11.0% ±0.5	0.05

2.2. Improvement of Spin-coated Fullerene ETLs in PSCs

Considering that the crystallinity of the C_{60} films leads to lower device performance, we added a small amount of C_{70} into the C_{60} solution to suppress the crystallinity of the spin-coated C_{60} film. C_{60}- and C_{70}- mixed fullerene films (referred to as "mixed fullerene films" hereafter) are reported to possess lower crystallinity than pure C_{60}.[47,48] Furthermore, the native C_{60} and C_{70} mixtures obtained during fullerene synthesis are considerably less expensive than the pure compounds.[49] GIXRD spectra in **Figure 2a** show that the mixed fullerene film exhibits much weaker (111) and

(220) peaks. TEM analysis also reveals that the mixed fullerene film (**Figure 2f**) displays suppressed crystallinity in contrast to the spin-coated C_{60} film (**Figure 2d**). This is evident from the selected-area electron diffraction ring patterns (SAED); the SAED pattern of the spin-coated C_{60} film (**Figure 2d inset, Figure S9e**) shows stronger crystallinity than that of the mixed fullerene film (**Figure 2f inset, Figure S9f**). Moreover, crystal domains were not observed in the mixed fullerene films (**Figure 2g, Figure S9d**). To the best of our knowledge, the low crystallinity of mixed fullerene has not been discussed in detail in the literature so far. We can explain this phenomenon in terms of their packing. Theoretically, C_{60} packing is more stable in a face-centered cubic (fcc) form (**Figure 2h**) than in a hexagonal close-packed (hcp) form, whereas C_{70} is more stable in the hcp form (**Figure 2i**).[50] However, in reality, C_{60} is present in both hcp and fcc forms, whereas C_{70} only exists in the hcp form.[51] Therefore, in mixed fullerenes, as C_{60} molecules attempt to form an fcc structure, C_{70} molecules existing between C_{60} molecules prevent the formation of fcc packing. For C_{60} in the hcp form, which is less stable, the larger and asymmetric C_{70} molecules distort the packing, inhibiting the crystallization. The morphologies of the films were investigated using the topography and adhesion modes of atomic force microscopy (AFM). The mixed fullerene film showed lower surface roughness with a roughness average (Ra) of 2.43 nm compared with the spin-coated C_{60} films, which showed the Ra of 7.19 nm (**Figure 3a and b**). We could also detect the crystal domain boundaries of the fullerene films by probing the adhesion of the film surface. From the high adhesion force of the crystal boundaries, we could conclude that the C_{60} films possessed many domains of *ca.* 50 nm (**Figure 3c**). In the case of mixed fullerene, the boundaries were much less defined (**Figure 3d**). This is evident from the 3D images in which the mixed fullerene films have much flatter topography.
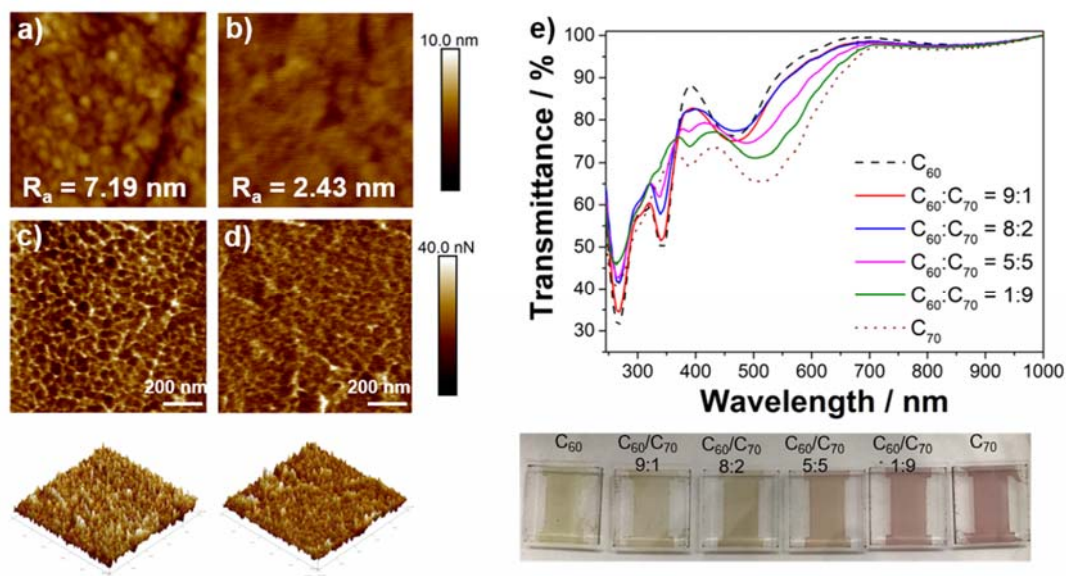
Figure 3. AFM topographic images of spin-coated a) C_{60} film and b) mixed fullerene film with roughness average values. AFM adhesion images of spin-coated c) C_{60} film and d) mixed fullerene film with the 3D images. e) Transmittance of fullerene films with different C_{60} to C_{70} ratios along with their pictures showing different colors.

PSCs with normal architecture were fabricated using the spin-coated mixed fullerene ETLs with different C_{60} to C_{70} ratios (**Table 2, Figure S7b**). The best PCE of 16.7% was achieved with the native C_{60} and C_{70} mixture ratio (C_{60}:C_{70} = 9:1 in weight). This PCE is as high as that of the thermally deposited C_{60}-based PSCs (**Table 1**). The devices with greater C_{70} content exhibited lower J_{SC} and lower FF (**Table 2**). UV–vis spectra with different C_{60}/C_{70} ratios showed that the increase in the amount of C_{70} reduces the transmittance of the film (**Figure 3e**), thus reducing the J_{SC}. The C_{60}/C_{70} films with the weight ratio 9:1 showed almost the same absorption as that of the pure C_{60}, as indicated by the similar J_{SC} values. The lowering trend of FF is observed because the charge transfer between C_{70} and the perovskite layer is not favored as discussed in section 2.1.1. We used solid-state ab initio calculations to assess the energy level change when C_{60} and C_{70} are mixed and the contributions from each component to the density of

states (DOS) in the conduction band. Solid-state calculations were performed at the dispersion-corrected density functional tight binding level (**Figure S3**). The DOS of C_{60} and C_{70} solids (**Figure S10a**) show the same energy levels to C_{60} and C_{70}, similar to the comparison at the single-molecule level in **Figure S3**. Mixing C_{60} and C_{70} yielded a similar result in that the energy contributions from C_{70} and C_{60} to the conduction band are similar (**Figure 1b, Figure S10b**), indicating that there is no LUMO offset within the mixed film, which could potentially inhibit charge transport. This is corroborated experimentally by the PYS measurement (**Figure S4e**). We also conducted simulations of selected low-index surfaces and confirmed that there is no change in DOS owing to the presence of the mixed fullerene interface (**Figure S11**). In addition, the ab initio calculations suggest that the mixed system is only approximately 0.03 eV/molecule above the convex hull (**Figure S12**), which is approximately kT at room temperature; there is, therefore, no significant driving force for segregation or desegregation. These results indicate that there is no significant change in the energy level when C_{70} is introduced, and the reduction in V_{OC} can be ascribed to the increase in charge recombination. Notably, all devices that used the mixed fullerenes showed a higher V_{OC} than pure C_{60} or C_{70} was applied. According to our computational results, it vividly demonstrated that the conjugation of the mixed C_{60} and C_{70} is much intact, providing a better interface for forming the perovskite at the interface with few voids, which thusly slightly increased the V_{OC} of devices. Consequently, we can conclude that the native mixed fullerene weight ratio of 9:1 is the optimized ratio, and mixing too much C_{70} undermines the device performance (**Figure 4a**).
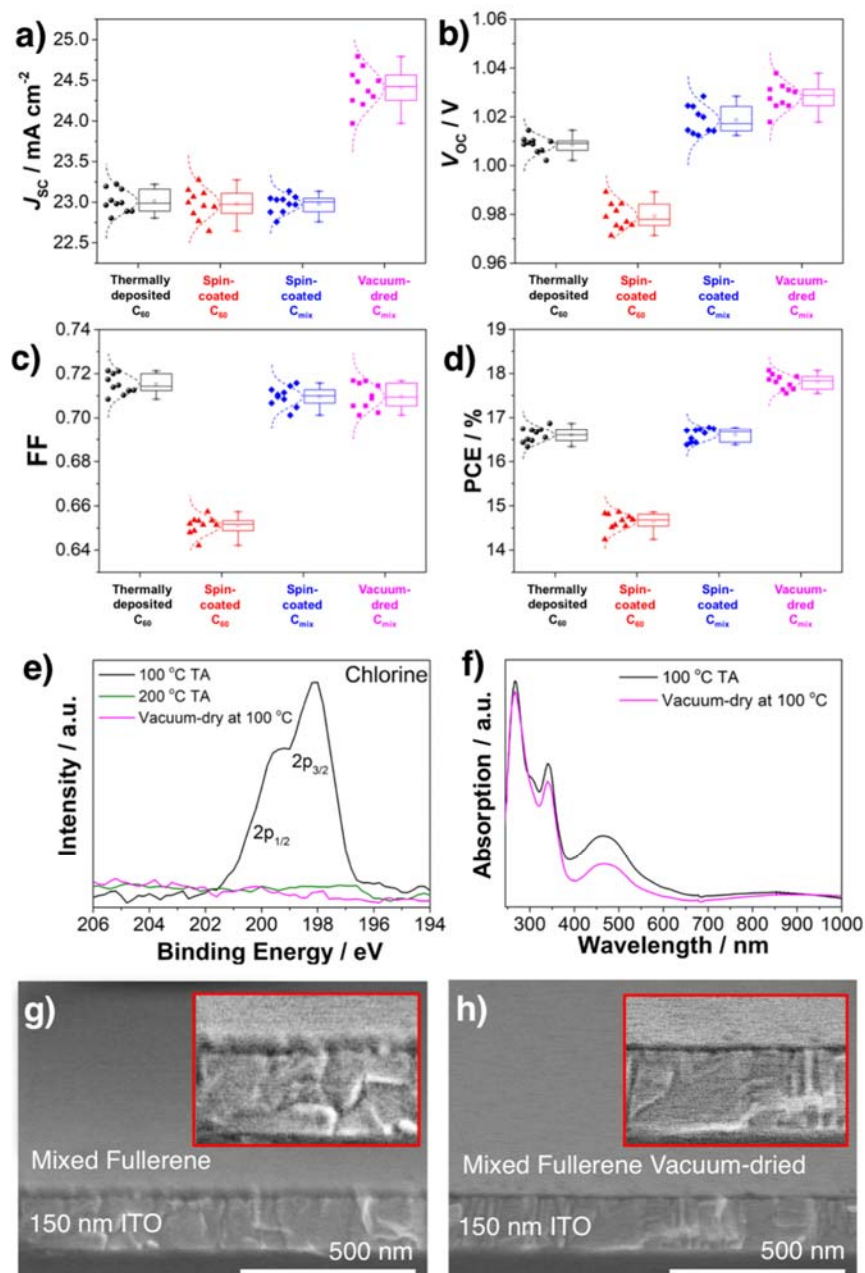
Figure 4. Photovoltaic parameters and statistical analysis of thermally deposited C_{60}-based PSCs (black circles), spin-coated C_{60}-based PSCs (red triangles), spin-coated mixed-fullerene-based PSCs (blue diamonds), and vacuum-dried mixed-fullerene-based PSCs (purple squares), showing a) J_{SC}, b) V_{OC}, c) FF, and d) PCE. e) XPS chlorine spectra of a mixed fullerene film thermally annealed at 100 °C (black), a mixed fullerene film thermally annealed at 200 °C (green), and a mixed fullerene film thermally annealed at 100 °C (purple) under vacuum. f) UV–vis absorption spectra of a mixed fullerene film thermally annealed at 100 °C (black) and a vacuum-dried mixed fullerene film (purple). Cross-sectional SEM pictures of spin-coated g) mixed fullerene film and h) the same film after vacuum-drying it on ITO substrates with magnified images as insets.

2.3. Further Enhancement of Mixed Fullerene ETL.

Considering that the mixed fullerene ETLs can achieve PCE as high as that of the thermally deposited C_{60} ETLs, we report a method to improve the PCE of these mixed fullerene ETLs even further. In addition to the amorphous state, a favorable aspect of the thermally evaporated C_{60} is that it is solvent-free. By removing the trapped solvents from the spin-coated mixed fullerene films, we postulate that the fullerenes can be packed in a more compact manner, improving the charge transport and eliminating the solvent effects.[52,53] To remove the ortho-dichlorobenzene (ODCB) effectively, we applied three different treatments to the spin-coated mixed fullerene films: thermal annealing (TA) at 100 °C, TA at 200 °C, and TA at 100 °C under a light vacuum (0.01 MPa). **Table 3** shows the photovoltaic performances of the PSCs with different post-treatments applied to the spin-coated mixed fullerene ETLs. The PSCs treated with TA at 100 °C did not exhibit a significant change in the device performance (**Figure S13**). We suspect that this temperature is not sufficiently high to remove ODCB (boiling point of 180 °C). In contrast, the PSCs treated with TA at 200 °C exhibited reduced device performance (**Table 3, Figure S13**). According to the AFM morphology analysis in **Figure S14a**, TA at 200 °C resulted in aggregation of the fullerene films. While such a high temperature is effective for removing ODCB, it leads to strong crystallization, which severely roughens the morphology as indicated by the low FF.[54,55] Finally, we vacuum-dried the film at 100 °C for 10 min. The device performance increased to 18.0% with the increase in J_{SC} and V_{OC} whereas FF remained the same (**Figure 4a, b, c, and d; Table 3; Figure S13**). The AFM roughness image and the corresponding Ra value reveal that the morphology of the fullerene film improved with the vacuum-drying treatment (**Figure S14b**). However, the improvement in morphology does not explain the improvements in J_{SC} and V_{OC}. X-ray photoelectron spectroscopy (XPS) was used to

confirm the removal of solvents via vacuum-drying. The data indicate that the chlorine from ODCB solvent, which was detectable in films treated with TA at 100 °C, was not detectable in the films treated with TA at 200 °C and vacuum-dried films (**Figure 4e**). UV–vis absorption spectra in **Figure 4f** indicate that the vacuum-drying treatment reduced the absorption of the film significantly. We conjecture that the removal of ODCB increased the transmittance of the film by removing solvatochromism.[54,55] Cross-sectional scanning electron microscope (SEM) image of the spin-coated mixed fullerene film, with a magnified image as an inset, shows that the fullerene film has a thickness of approximately 32 nm (**Figure 4g**), which is similar to the optimized thickness i.e., 35 nm of the thermally deposited C_{60} film (**Figure S15**). After the vacuum-drying treatment, we can observe that the thickness of the same mixed fullerene film decreased to *ca.* 12 nm (**Figure 4h**). GIXRD spectra showed a decrease in the crystallinity of the spin-coated mixed fullerene films upon vacuum-drying treatment, thus resembling the thermally evaporated C_{60} film (**Figure S8**). This confirms that the removal of solvent affected the packing and crystallinity of the fullerenes. The combination of enhanced transmittance and charge transport led to the increase in J_{SC} and V_{OC}. Ultimately, the PCE of the vacuum-dried solution-processed mixed-fullerene-based PSC (18.0%) exceeded that of the thermally evaporated C_{60}-based PSC (16.7%). Moreover, this vacuum-dry method can be applied to other solution-processed fullerene ETLs such as C_{60} and C_{70}, which gave a better performance than none treated devices (Table S2, Figure S16). For instance, the vacuum-dried solution-processed C_{60} achieved a PCE in 16.0%, exceeding non-treated solution-processed C_{60} with a PCE in 14.8%. The vacuum-dried solution-processed C_{70} (12.1%) slightly exceed the non-treated solution-processed C_{70} (11.7%).

Table 3. Photovoltaic parameters of the normal-type PSCs using mixed fullerene as the ETL with different film treatments under one sun (AM 1.5 G, 100 mW cm^{-2}).

Fullerene	Treatment	J_{SC} [mA cm^{-2}]	V_{OC} [V]	FF	R_S [Ω cm^2]	R_{SH} [Ω cm^2]	PCE$_{Best}$	PCE$_{Average}$	Hysteresis Index
Spin-coated C$_{60}$/C$_{70}$ (9:1)	none	22.9	1.02	0.71	42	1.7x10^4	16.7%	16.6% ±0.5	0.04
	100 °C TA	23.2	1.04	0.71	33	1.7x10^3	16.9%	16.0% ±0.4	0.04
	200 °C TA	22.5	1.05	0.66	20	4.0x10^3	15.7%	14.8% ±1.0	0.13
	Vacuum-dry at 100 °C	24.3	1.03	0.73	28	1.5x10^4	18.0%	17.7% ±0.6	0.01

3. CONCLUSIONS

We compared C$_{60}$ and C$_{70}$ in PSCs. The comparison was extended to thermally evaporated and solution-processed deposition methods of fullerenes in normal and inverted architectures of PSCs. C$_{60}$ as ETL in PSC exhibited higher photovoltaic performance than C$_{70}$. The thermally deposited C$_{60}$-based normal-type PSCs showed a PCE of 16.7%. By investigating the mechanism behind the efficiency enhancement, we discovered that the high performance of the thermally deposited C$_{60}$-based PSCs is attributed to the crystallinity of the fullerene and the presence of remnant solvents. By mixing a small amount of C$_{70}$ into a solution of C$_{60}$, the crystallinity of the spin-coated fullerene films decreased substantially, resulting in a PCE close to that of the thermally deposited C$_{60}$-based PSCs. Furthermore, by vacuum-drying the mixed fullerene film, a PCE of 18% without hysteresis was achieved, which exceeds that of the thermally deposited C$_{60}$-based PSCs.

4. EXPERIMENTAL

Mixed-fullerene solution preparation. C_{60} and C_{70} were dissolved in a solution of ODCB in different ratios with a mass concentration of 20.0 mg mL^{-1}. The solution was filtered through a 0.45 μm polytetrafluoroethylene filter prior to use.

Spiro-MeOTAD solution preparation. A solution was prepared by mixing 85.8 mg spiro-MeOTAD (Lumtech), 19.3 μL of a stock solution of 520 mg mL^{-1} lithium bis(trifluoromethylsulphonyl)imide (Aldrich) in anhydrous acetonitrile, and 33.8 μL of 4-*tert*-butylpyridine (Aldrich) in 1 mL anhydrous chlorobenzene.

PEDOT:PSS solution preparation. Poly(3,4-ethylenedioxythiophene) polystyrene sulfonate (PEDOT:PSS) solution was produced by adding 0.5 wt% polyoxyethylene(6) tridecyl ether (Sigma-Aldrich Chemical Co., Inc.) to a PEDOT:PSS dispersion in water (Clevios P VP, Heraeus Precious Metals GmbH & Co.). The solution was filtered through a 0.45 μm polytetrafluoroethylene filter prior to use.

Perovskite (MAPbI$_3$) precursor solution preparation. CH_3NH_3I (TCI), PbI_2 (TCI), and anhydrous dimethyl sulfoxide (TCI) (molar ratio 1:1:1) were mixed in anhydrous *N,N*-dimethylformamide (TCI) with a concentration of 50 wt%. The solution was filtered through a 0.45 μm polytetrafluoroethylene filter prior to use.

Fabrication of inverted-type planar heterojunction perovskite solar cells. Indium tin oxide (ITO) patterned glass substrates with a size of 15×15 mm^2 and sheet resistance of 6 Ω sq^{-1} (Techno Print Co., Ltd.) were cleaned and sonicated with a detergent, distilled water, acetone, and isopropanol in an ultrasonic bath for 15 min. Subsequently, the substrates were treated with ultraviolet/ozone (UV/O$_3$) for 15 min prior to use. Thereafter, 25 µL of PEDOT:PSS solution was spin-coated on UV/O$_3$-treated ITO substrates at 3000 rpm for 30 s. The coated ITO substrates were subsequently annealed at 105 °C for 10 min. Thereafter, 25 µL of the perovskite precursor solution was spin-coated on the PEDOT:PSS layer at 3000 rpm for 30 s, and 0.5 mL of anhydrous diethyl ether was slowly dripped onto the substrate 10 s after the start of the spin-coating process. Subsequently, the film was annealed at 100 °C for 10 min to obtain a dense brown MAPbI$_3$ film. Subsequently, C$_{60}$ or C$_{70}$ was thermally deposited on the perovskite film to obtain a thickness of 30 nm at a constant evaporation rate of 0.02 nm s^{-1}. Similarly, bathocuproine was thermally deposited to obtain a thickness of 10 nm at the same evaporation rate. Finally, a 70-nm-thick Ag cathode was fabricated via thermal deposition at a constant evaporation rate of 0.05 nm s^{-1}.

Fabrication of normal type planar heterojunction perovskite solar cells. ITO patterned glass substrates were cleaned and sonicated with detergent, distilled water, acetone and isopropanol in an ultrasonic bath for 15 min, respectively. Subsequently, 25 µL of mix-fullerene solution was spin-coated on ITO substrates at 3000 rpm for 30 s. The coated ITO substrates were used without any treatment or were followed by different processes, such as: 1) annealing at 100°C for 1 h; 2) annealing at 200 °C for 1 h; 3) drying up at 100°C under vacuum condition ($\sim 1.0 \times 10^{-3}$ MPa) for 1 h. If thermally deposited fullerene film was used, C$_{60}$ or C$_{70}$ was thermally deposited on ITO substrates in a thickness of 30 nm at a constant evaporation rate of 0.02 nm s^{-1}.

Then, 25 μL of perovskite precursor solution was spin-coated on the fullerene layer at 3000 rpm for 30 s, with a dropping of 0.5 mL of anhydrous diethyl ether was slowly dripped onto the substrate 10 s after the start of the spin-coating process. Next, the film was annealed at 100 °C for 10 min to obtain a dense brown $MAPbI_3$ film. The hole transporting layer was spin-coated from the spiro-MeOTAD solution at 4000 rpm for 30 s. Finally, a 70-nm-thick of Au anode was fabricated by thermal deposition at a constant evaporation rate of 0.05 nm s^{-1}.

Characterizations. The *J–V* characteristics were measured using a software-controlled source meter (Keithley 2400 SourceMeter) under dark conditions and the simulated sunlight irradiation of 1 sun (AM 1.5G; 100 mW cm^{-2}) using a solar simulator (EMS-35AAA, Ushio Spax Inc.) with a Ushio Xe short arc lamp 500. The source meter was calibrated using a silicon diode (BS-520BK, Bunkokeiki). SEM analysis of the perovskite films was performed using an S-4800 (Hitachi). The TEM images are taken by JEM-2010F (JEOL Ltd.) with a thermal field emission gun operated at 200 keV. The Selected area electron diffraction (SAED) patterns are recorded by a Charge-coupled Device (CCD) at a camera length of 60 cm.

Shimadzu UV-3150 was used for the UV–vis–NIR measurement. The PL measurements were performed using JASCO Spectrofluorometer (FP-8300). Topography images were recorded by using an atomic force microscope (AFM) operating in tapping mode (SPI3800N, SII). The grazing-incidence XRD 2θ scans were performed on a Jordan Valley D1 diffractometer with copper Kα$_1$ radiation and a parallel beam source. In the 2θ scans, the scattering angle 2θ between incident beam and diffracted beam changes while the incident angle ω between incident beam and the sample surface is fixed at 1 degree. The valence band and Fermi levels measurements were performed using Riken Keiki PYS-A AC-2 and Kelvin probe spectroscopy in air (ESA), respectively. The photoemission measurements were performed using XPS (PHI5000, Versa

Probe) with monochromatic Al Kα radiation. The water contact angle measurements were performed using a contact angle meter (DMo-501, Kyowa Interface Science Co., Ltd.).

ASSOCIATED CONTENT

Supporting Information.

Cross sectional SEM, device fabrication, various computational calculations, PYS, UV-vis absorption, GIXRD, TEM, AFM.

AUTHOR INFORMATION

Corresponding Author

*I.J: il.jeon@spc.oxon.org, *Y.M: matsuo@photon.t.u-tokyo.ac.jp

Author Contributions

H.L and I.J conceived the experiment. H.L and S.S conducted device fabrication. R.X carried out TEM analyses. J.L and Y.Y carried out AFM analyses. C.L and M.G carried out GIXRD analyses. A.P and S.M conducted computational analyses. H.L, I.J, S.M, and Y.M did the rest of the analyses and the related discussion. H.L and I.J wrote the manuscript.

REFERENCES

(1)   Green, M. A.; Ho-Baillie, A.; Snaith, H. J. The emergence of perovskite solar cells. *Nat. Photonics* **2014**, *8*, 506–514.

(2)   Kazim, S.; Nazeeruddin, M. K.; Grätzel, M.; Ahmad, S. Perovskite as light harvester: a game changer in photovoltaics. *Angew. Chem., Int. Ed. Engl.* **2014**, *53*, 2812–2824.

(3)   Shin, S. S.; Yeom, E. J.; Yang, W. S.; Hur, S.; Kim, M. G.; Im, J.; Seo, J.; Noh, J. H.; Seok, S. I. Colloidally prepared La-doped $BaSnO_3$ electrodes for efficient, photostable perovskite solar cells. *Science* **2017**, *356*, 167–171.

(4)   Lee, J.-W.; Seol, D.-J.; Cho, A.-N.; Park, N.-G. High-efficiency perovskite solar cells based on the black polymorph of $HC(NH_2)_2PbI_3$ *Adv. Mater.* **2014**, *26*, 4991–4998.

(5)   Correa-Baena, J.-P.; Saliba, M.; Buonassisi, T.; Grätzel, M.; Abate, A.; Tress, W.; Hagfeldt, A. Promises and challenges of perovskite solar cells *Science* **2017**, *358*, 739–744.

(6)   Gatti, T.; Menna, E.; Meneghetti, M.; Maggini, M.; Petrozza, A.; Lamberti, F. The renaissance of fullerenes with perovskite solar cells *Nano Energy* **2017**, *41*, 84–100.

(7)   You, J.; Meng, L.; Hong, Z.; Li, G.; Yang, Y. *Organic-Inorganic Halide Perovskite Photovoltaics*; Springer International Publishing: Cham, 2016; pp. 307–324.

(8)   Liang, P.-W.; Chueh, C.-C.; Williams, S. T.; Jen, A. K.-Y. Roles of fullerene-based interlayers in enhancing the performance of organometal perovskite thin-film solar cells *Adv. Energy Mater.* **2015**, *5*, 1402321.

(9)   Xie, Y.; Li, Y.; Xiao, L.; Qiao, Q.; Dhakal, R.; Zhang, Z.; Gong, Q.; Galipeau, D.; Yan, X. Femtosecond time-resolved fluorescence study of P3HT/PCBM blend films *J. Phys. Chem. C* **2010**, *114*, 14590–14600.

(10)   von Hauff, E.; Dyakonov, V.; Parisi, J. Study of field effect mobility in PCBM films and P3HT:PCBM blends *Sol. Energy Mater. Sol. Cells* **2005**, *87*, 149–156.

(11)   a) Wei, J.; Zhao, Y.; Li, H.; Li, G.; Pan, J.; Xu, D.; Zhao, Q.; Yu, D. Hysteresis analysis based on the ferroelectric effect in hybrid perovskite solar cells *J. Phys. Chem. Lett.* **2014**, *5*, 3937–3945; b) Lee, J.-W.; Kim, S.-G.; Bae, S.-H.; Lee, D.-K.; Lin, O.; Yang, Y.; Park, N.-G. The interplay between trap density and hystersis in plannar heterojunction perovskit solar cells, *Nano Lett.* **2017**, *17*, 4270–4276.

(12)   Snaith, H. J.; Abate, A.; Ball, J. M.; Eperon, G. E.; Leijtens, T.; Noel, N. K.; Stranks, S. D.; Wang, J. T.-W.; Wojciechowski, K.; Zhang, W. Anomalous hysteresis in perovskite solar cells *J. Phys. Chem. Lett.* **2014**, *5*, 1511–1515.

(13)   Leijtens, T.; Eperon, G. E.; Pathak, S.; Abate, A.; Lee, M. M.; Snaith, H. J. Overcoming ultraviolet light instability of sensitized TiO_2 with meso-superstructured organometal tri-halide perovskite solar cells *Nat. Commun.* **2013**, *4*, 2885.

(14)   Ito, S.; Tanaka, S.; Manabe, K.; Nishino, H. Effects of surface blocking layer of Sb_2S_3 on nanocrystalline TiO_2 for $CH_3NH_3PbI_3$ perovskite solar cells *J. Phys. Chem. C* **2014**, *118*, 16995–17000.

(15)   Jeon, I.; Chiba, T.; Delacou, C.; Guo, Y.; Kaskela, A.; Reynaud, O.; Kauppinen, E. I.; Maruyama, S.; Matsuo, Y. Single-walled carbon nanotube film as electrode in indium-free planar heterojunction perovskite solar cells: investigation of electron-blocking layers and dopants *Nano Lett.* **2015**, *15*, 6665–6671.

(16)   Jeon, I.; Yoon, J.; Ahn, N.; Atwa, M.; Delacou, C.; Anisimov, A.; Kauppinen, E. I.; Choi, M.; Maruyama, S.; Matsuo, Y. carbon nanotubes versus graphene as flexible transparent electrodes in inverted perovskite solar cells *J. Phys. Chem. Lett.* **2017**, *8*, 5395–5401.

(17)   Tao, C.; Neutzner, S.; Colella, L.; Marras, S.; Srimath Kandada, A. R.; Gandini, M.; De Bastiani, M.; Pace, G.; Manna, L.; Caironi, M.; Bertarelli, C.; Petrozza, A. 17.6% stabilized efficiency in low-temperature processed planar perovskite solar cells *Energy Environ. Sci.* **2015**, *8*, 2365–2370.

(18)   Ke, W.; Zhao, D.; Grice, C. R.; Cimaroli, A. J.; Ge, J.; Tao, H.; Lei, H.; Fang, G.; Yan, Y. Efficient planar perovskite solar cells using room-temperature vacuum-processed C60 electron selective layers *J. Mater. Chem. A* **2015**, *3*, 17971–17976.

(19)   Ahn, N.; Jeon, I.; Yoon, J.; Kauppinen, E. I.; Matsuo, Y.; Maruyama, S.; Choi, M. Carbon-sandwiched perovskite solar cell *J. Mater. Chem. A* **2018**, *6*, 1382–1389.

(20)   Ahn, N.; Kwak, K.; Jang, M. S.; Yoon, H.; Lee, B. Y.; Lee, J.-K.; Pikhitsa, P. V.; Byun, J.; Choi, M. Trapped charge-driven degradation of perovskite solar cells *Nat. Commun.* **2016**,

7, 13422.

(21)   Xu, J.; Buin, A.; Ip, A. H.; Li, W.; Voznyy, O.; Comin, R.; Yuan, M.; Jeon, S.; Ning, Z.; McDowell, J. J.; Kanjanaboos, P.; Sun, J.-P.; Lan, X.; Quan, L. N.; Kim, D. H.; Hill, I. G.; Maksymovych, P.; Sargent, E. H. Perovskite–fullerene hybrid materials suppress hysteresis in planar diodes *Nat. Commun.* **2015**, *6*, 7081.

(22)   Shao, Y.; Xiao, Z.; Bi, C.; Yuan, Y.; Huang, J. Origin and elimination of photocurrent hysteresis by fullerene passivation in $CH_3NH_3PbI_3$ planar heterojunction solar cells *Nat. Commun.* **2014**, *5*, 5784.

(23)   Zhao, D.; Ke, W.; Grice, C. R.; Cimaroli, A. J.; Tan, X.; Yang, M.; Collins, R. W.; Zhang, H.; Zhu, K.; Yan, Y. Annealing-free efficient vacuum-deposited planar perovskite solar cells with evaporated fullerenes as electron-selective layers *Nano Energy* **2016**, *19*, 88–97.

(24)   Ha, J.; Kim, H.; Lee, H.; Lim, K.-G.; Lee, T.-W.; Yoo, S. Device architecture for efficient, low-hysteresis flexible perovskite solar cells: Replacing TiO_2 with C_{60} assisted by polyethylenimine ethoxylated interfacial layers *Sol. Energy Mater. Sol. Cells* **2017**, *161*, 338–346.

(25)   Lee, K.-M.; Chen, C.-C.; Chen, L.-C.; Chang, S. H.; Chen, K.-S.; Yeh, S.-C.; Chen, C.-T.; Wu, C.-G. Thickness effects of thermally evaporated C_{60} thin films on regular-type $CH_3NH_3PbI_3$ based solar cells *Sol. Energy Mater. Sol. Cells* **2017**, *164*, 13–18.

(26)   Collavini, S.; Kosta, I.; Völker, S. F.; Cabanero, G.; Grande, H. J.; Tena-Zaera, R.; Delgado, J. L. Efficient regular perovskite solar cells based on pristine [70]fullerene as electron-selective contact *ChemSusChem* **2016**, *9*, 1263–1270.

(27) Zhang, K.; Yu, H.; Liu, X.; Dong, Q.; Wang, Z.; Wang, Y.; Chen, N.; Zhou, Y.; Song, B. Fullerenes and derivatives as electron transport materials in perovskite solar cells *Sci. China Chem.* **2017**, *60*, 144–150.

(28) Heumueller, T.; Burke, T. M.; Mateker, W. R.; Sachs-Quintana, I. T.; Vandewal, K.; Brabec, C. J.; McGehee, M. D. Disorder-induced open-circuit voltage losses in organic solar cells during photoinduced burn-in *Adv. Energy Mater.* **2015**, *5*, 1500111.

(29) Blakesley, J. C.; Neher, D. Relationship between energetic disorder and open-circuit voltage in bulk heterojunction organic solar cells *Phys. Rev. B* **2011**, *84*, 075210.

(30) Wu, Y.; Yang, X.; Chen, W.; Yue, Y.; Cai, M.; Xie, F.; Bi, E.; Islam, A.; Han, L. Perovskite solar cells with 18.21% efficiency and area over $1\,cm2$ fabricated by heterojunction engineering *Nat. Energy* **2016**, *1*, 16148.

(31) Pal, A.; Wen, L. K.; Jun, C. Y.; Jeon, I.; Matsuo, Y.; Manzhos, S. Comparative density functional theory–density functional tight binding study of fullerene derivatives: effects due to fullerene size, addends, and crystallinity on band structure, charge transport and optical properties *Phys. Chem. Chem. Phys.* **2017**, *19*, 28330–28343.

(32) Becke, A. D. A new mixing of Hartree–Fock and local density-functional theories *J. Chem. Phys.* **1993**, *98*, 1372.

(33) Hosoya, M.; Ichimura, K.; Wang, Z. H.; Dresselhaus, G.; Dresselhaus, M. S.; Eklund, P. C. Dark conductivity and photoconductivity in solid films of C_{70}, C_{60} and K_xC_{70} *Phys. Rev. B* **1994**, *49*, 4981.

(34) Hassan Bhuiyan, M. K.; Mieno, T. Effect of oxygen on electric conductivities of C60 and

higher fullerene thin films *Thin Solid Films* **2003**, *441*, 187–191.

(35) Haddon, R. C. C$_{70}$ Thin Film Transistors *J. Am. Chem. Soc.* **1996**, *118*, 3041–3042.

(36) Xi, X.; Li, W.; Wu, J.; Ji, J.; Shi, Z.; Li, G. A comparative study on the performances of small molecule organic solar cells based on CuPc/C$_{60}$ and CuPc/C$_{70}$ *Sol. Energy Mater. Sol. Cells* **2010**, *94*, 2435–2441.

(37) de Quilettes, D. W.; Vorpahl, S. M.; Stranks, S. D.; Nagaoka, H.; Eperon, G. E.; Ziffer, M. E.; Snaith, H. J.; Ginger, D. S. Impact of microstructure on local carrier lifetime in perovskite solar cells *Science* **2015**, *348*, 683–686.

(38) Pascual, J.; Kosta, I.; Palacios-Lidon, E.; Chuvilin, A.; Grancini, G.; Nazeeruddin, M. K.; Grande, H. J.; Delgado, J. L.; Tena-Zaera, R. Co-solvent effect in the processing of the perovskite:fullerene blend films for electron transport layer-free solar cells *J. Phys. Chem. C* **2018**, *122*, 2512–2520.

(39) Zhang, X.; Ai, X.; Zhang, R.; Ma, Q.; Wang, Z.; Qin, G.; Wang, J.; Wang, S.; Suzuki, K.; Miyazaki, T.; Mizukami, S. Spin conserved electron transport behaviors in fullerenes (C$_{60}$ and C$_{70}$) spin valves *Carbon* **2016**, *106*, 202–207.

(40) Gao, M.; Zhang, H. Preparation of an amorphous fullerene film *Phys. Lett. A* **1996**, *213*, 203–206.

(41) Weaver, J. H.; Martins, J. L.; Komeda, T.; Chen, Y.; Ohno, T. R.; Kroll, G. H.; Troullier, N.; Haufler, R. E.; Smalley, R. E. Electronic structure of solid C$_{60}$: experiment and thory *Phys. Rev. Lett.* **1991**, *66*, 1741.

(42) Krakow, W.; Rivera, N. M.; Roy, R. A.; Ruoff, R. S.; Cuomo, J. J. Infrared-infrared

double-resonance spectra involving fermi perturbed levels and CO stretch band transitions of CD$_3$OH *Appl. Phys. A* **1993**, *56*, 185–191.

(43) Zaumseil, J.; Sirringhaus, H. Electron and ambipolar transport in organic field-effect transistors *Chem. Rev.* **2007**, *107*, 1296–1323.

(44) Ahn, K.; Kim, J. B.; Park, H.; Kim, H.; Lee, M. H.; Kim, B. J.; Cho, J. H.; Kang, M. S.; Lee, D. R. Enhancing crystallinity of C$_{60}$ layer by thickness-control of underneath pentacene layer for high mobility C$_{60}$/pentacene ambipolar transistors *Appl. Phys. Lett.* **2013**, *102*, 043306.

(45) Meng, Q.; Dong, H.; Hu, W.; Zhu, D. Recent progress of high performance organic thin film field-effect transistors *J. Mater. Chem.* **2011**, *21*, 11708–11721.

(46) Li, J.; Komiya, S.; Tamura, T.; Nagasaki, C.; Kihara, J.; Kishio, K.; Kitazawa, K. Growth and properties of pure C$_{60}$ fullerene single crystals from vapor *Phys. C: Supercond.* **1992**, *195*, 205–208.

(47) Sin, L. Y. M.; Tang, T. B.; Pai, W. W. Structural transformation of mixed C$_{60}$ and C$_{70}$ fullerene monolayer on Ag(100) *Jpn. J. Appl. Phys.* **2006**, *45*, 2377–2381.

(48) Uemura, S.; Taniguchi, I.; Sakata, M.; Kunitake, M. Electrochemical STM investigation of C$_{70}$, C$_{60}$/C$_{70}$ mixed fullerene and hydrogenated fullerene adlayers on Au(1 1 1) prepared using the electrochemical replacement method *J. Electroanal. Chem.* **2008**, *623*, 1–7.

(49) Andersson, L. M.; Hsu, Y.-T.; Vandewal, K.; Sieval, A. B.; Andersson, M. R.; Inganäs, O. Mixed C$_{60}$/C$_{70}$ based fullerene acceptors in polymer bulk-heterojunction solar cells *Org. Electron.* **2012**, *13*, 2856–2864.

(50) Guo, Y.; Karasawa, N.; III Goddard, W. A. Prediction of fullerene packing in C_{60} and C_{70} crystals *Nature* **1991**, *351*, 464–467.

(51) Dietz, P.; Fostiropoulos, K.; Krätschmer, W.; Hansma, P. K. Size and packing of fullerenes on C_{60}/C_{70} crystal surfaces studied by atomic force microscopy *Appl. Phys. Lett.* **1992**, *60*, 62–64.

(52) Gorun, S. M.; Creegan, K. M.; Sherwood, R. D.; Cox, D. M.; Day, V. W.; Day, C. S.; Upton, R. M.; Briant, C. E. Solvated fullerenes C_{60} and C_{60}/C_{70} and the low-resolution single crystal x-ray structure of C_{60} *J. Chem. Soc., Chem. Commun.* **1991**, 1556–1558.

(53) Jargalan, N.; Tropin, T. V.; Avdeev, M. V.; Aksenov, V. L. Investigation of the dissolution kinetics of fullerene C_{60} in solvents with different polarities by UV-Vis spectroscopy *J. Surf. Investig. X-ray, Synchrotron Neutron Tech.* **2015**, *9*, 12–16.

(54) Wu, W.-R.; Jeng, U.-S.; Su, C.-J.; Wei, K.-H.; Su, M.-S.; Chiu, M.-Y.; Chen, C.-Y.; Su, W.-B.; Su, C.-H.; Su, A.-C. Competition between fullerene aggregation and poly(3-hexylthiophene) crystallization upon annealing of bulk heterojunction Solar Cells *ACS Nano* **2011**, *5*, 6233–6243.

(55) Anthopoulos, T. D.; Singh, B.; Marjanovic, N.; Sariciftci, N. S.; Montaigne Ramil, A.; Sitter, H.; Cölle, M.; de Leeuw, D. M. *Appl. Phys. Lett.* **2006**, *89*, 213504.

Table of Contents
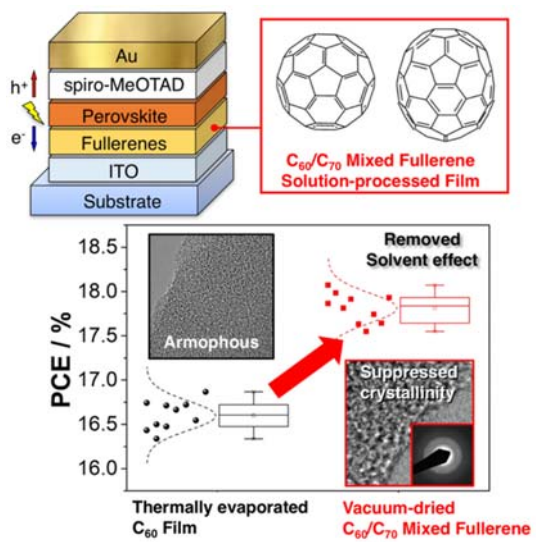
Supporting Information

Achieving High Efficiency in Solution-Processed

Perovskite Solar Cells using C_{60}/C_{70} Mixed Fullerenes

Hao-Sheng Lin[1], Il Jeon[1]*, Rong Xiang[1], Seungju Seo[1], Jin-Wook Lee[2], Chao Li[2], Amrita Pal[3],

Sergei Manzhos[3], Mark S.Goorsky[2], Yang Yang[2], Shigeo Maruyama[1], and Yutaka Matsuo[1,4]*

[1]Department of Mechanical Engineering, The University of Tokyo, 7-3-1 Hongo, Bunkyo-ku, Tokyo 113-8656, Japan

[2]Department of Materials Science and Engineering, University of California, Los Angeles, Los Angeles, CA 90095, USA

[3]Department of Mechanical Engineering, National University of Singapore, Block EA #07-08, 9 Engineering Drive 1, Singapore 117576, Singapore

[4]Hefei National Laboratory for Physical Sciences at the Microscale, University of Science and Technology of China, Hefei, Anhui 230026, China

*corresponding to il.jeon@spc.oxon.org (I.J) and matsuo@photon.t.u-tokyo.ac.jp (Y.M)
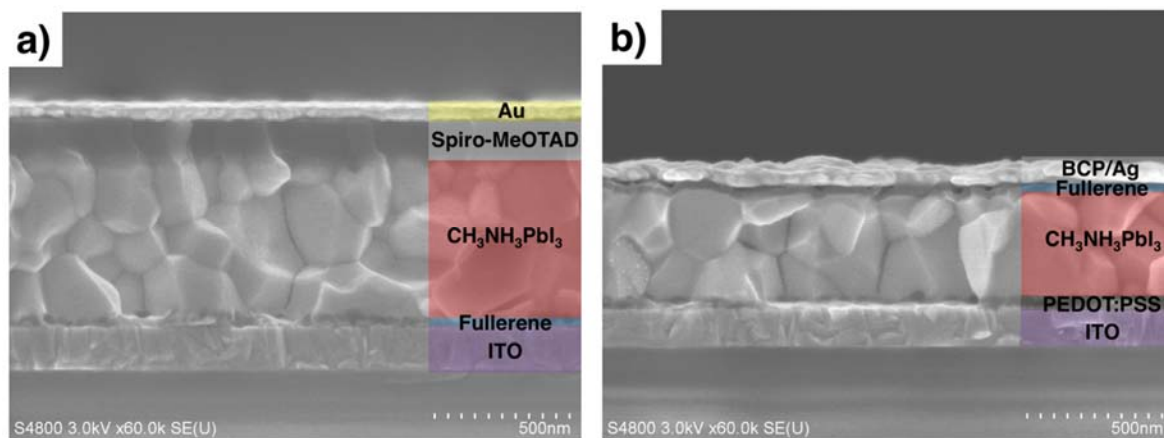
Figure S1. Cross-sectional SEM images of a) normal-type PSCs and b) inverted-type PSCs.
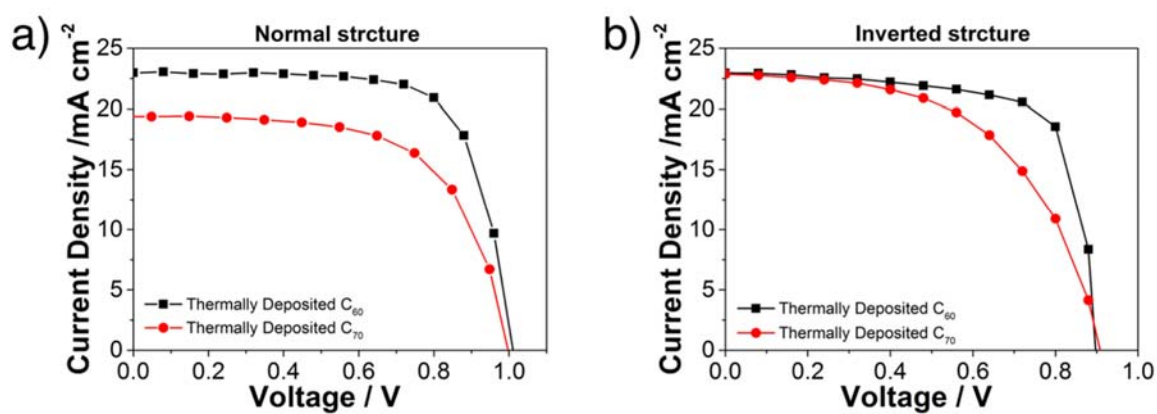
Figure S2. *J–V* curves of the thermally deposited C_{60}- (black squares and line) and C_{70}- (red circles and line) based PSC for a) the normal-type structure and b) the inverted-type structure.

a) Frontier orbital comparison of single molecules at the DFT level: [6-31+G(d,p)]

The calculations were performed in Gaussian 09[S1] with the 6-31+g(d,p) basis, in vacuum.

HOMO-LUMO distributions:
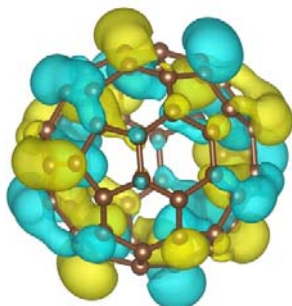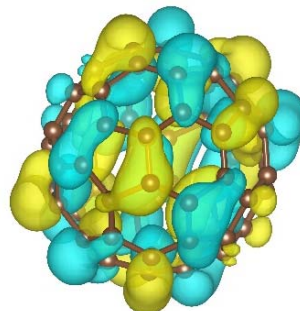
C_{60} HOMO   LUMO
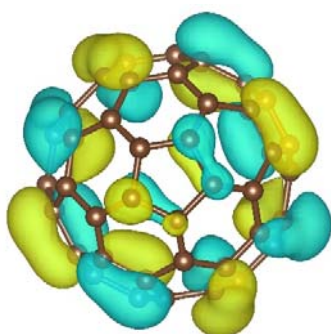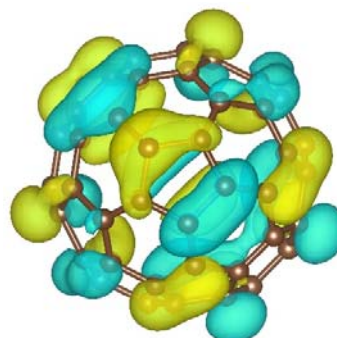
C_{70} HOMO   LUMO

The HOMO-LUMO values are as below:

With the B3LYP[S2] functional (quantitative)

C_{60}: HOMO: -6.40 eV C_{70}: HOMO: -6.33 eV

LUMO: -3.68 eV   LUMO: -3.67 eV

With the PBE[S3] functional (for comparison to DFTB)

C_{60}: HOMO: -5.86 eV C_{70}: HOMO: -5.86 eV

LUMO: -4.21 eV   LUMO: -4.16 eV

b) Energy level comparison of single molecules at the DFTB level:

The calculations were performed in DFTB+[S4] using the 3ob-3-1[S5,S6] parameter set

The HOMO-LUMO distributions:

C_{60} HOMO   LUMO
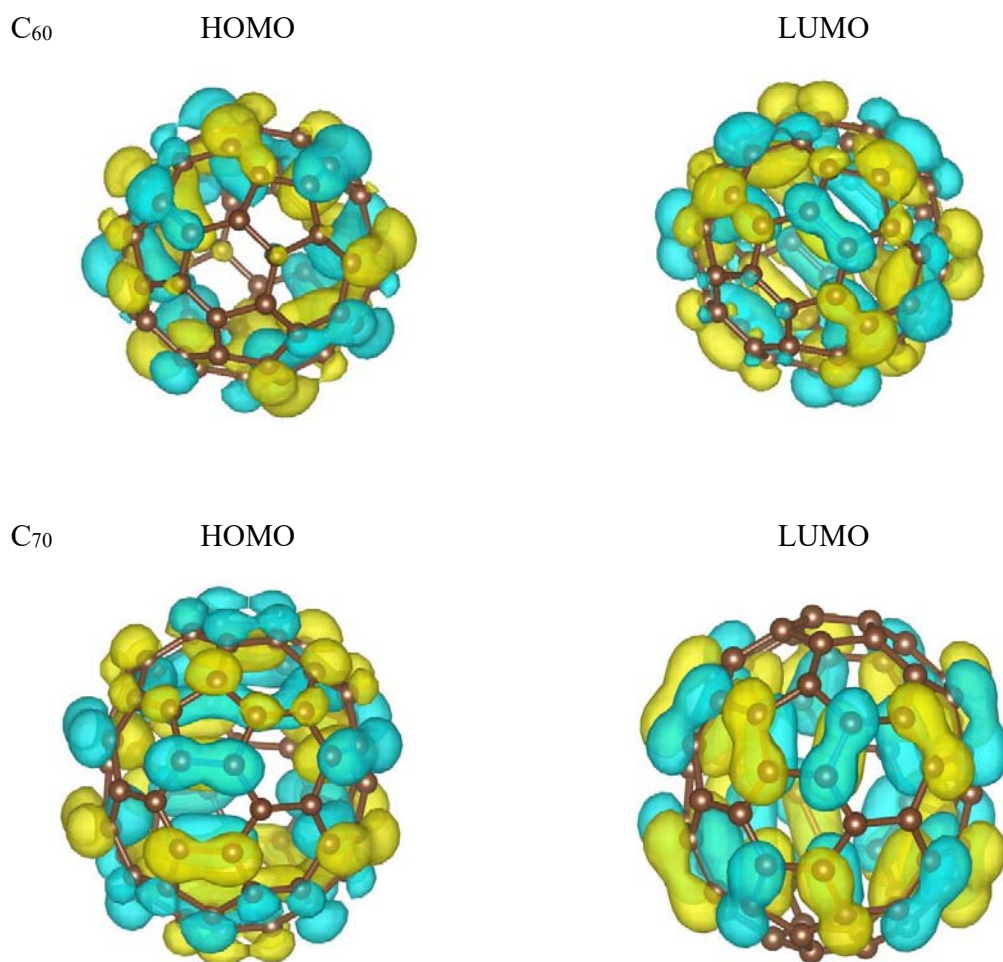
C_{70} HOMO   LUMO

The HOMO-LUMO values are as below:

C_{60}: HOMO: -5.67 eV C_{70}: HOMO: -5.60 eV

LUMO: -3.88 eV   LUMO: -3.97 eV

Figure S3. Frontier orbital calculations of C_{60} and C_{70} a) at the DFT level, and b) at the DFTB level.
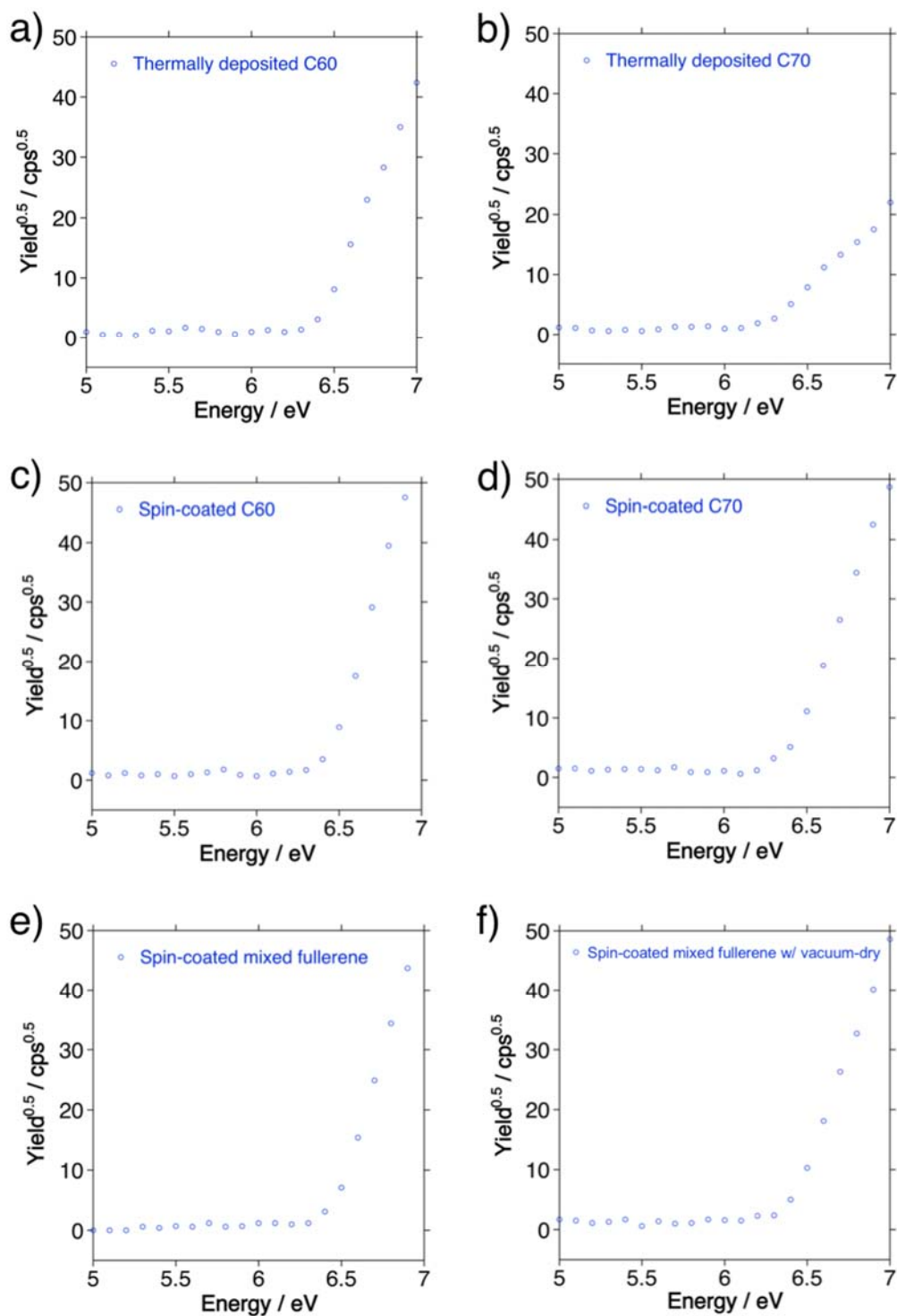
Figure S4. PYS spectra of a) thermally deposited C_{60}, b) thermally deposited C_{70}, c) spin-coated C_{60}, d) spin-coated C_{70}, e) spin-coated C_{60}/C_{70} (9:1), and f) vacuum-dried spin-coated C_{60}/C_{70} (9:1).

Figure S5. Various C_{60} and C_{70} films on glass and silicon substrates. The difference in transparency between C_{60} and C_{70} of the same thickness is visible even for the naked eye.
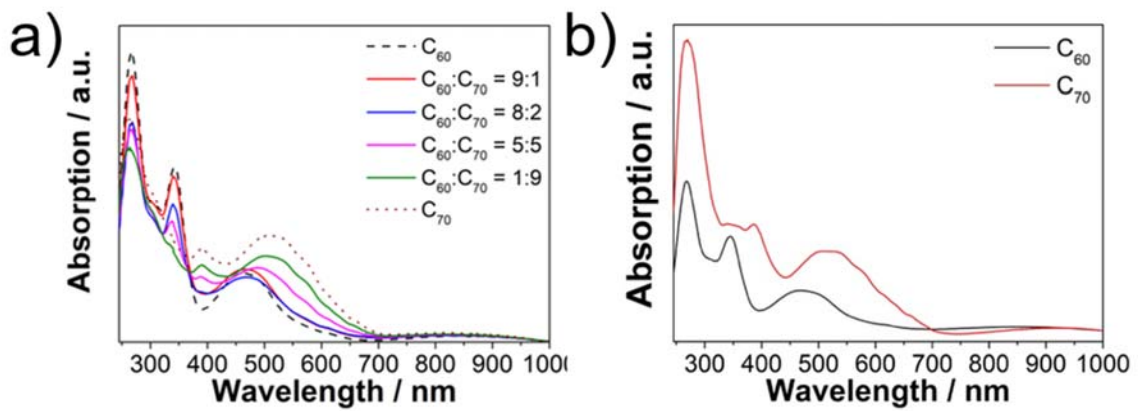
Figure S6. a) UV-vis absorption of spin-coated fullerene films with different C_{60} to C_{70} ratios. b) UV-vis absorption spectroscopy of thermally deposited C_{60} and C_{70}.
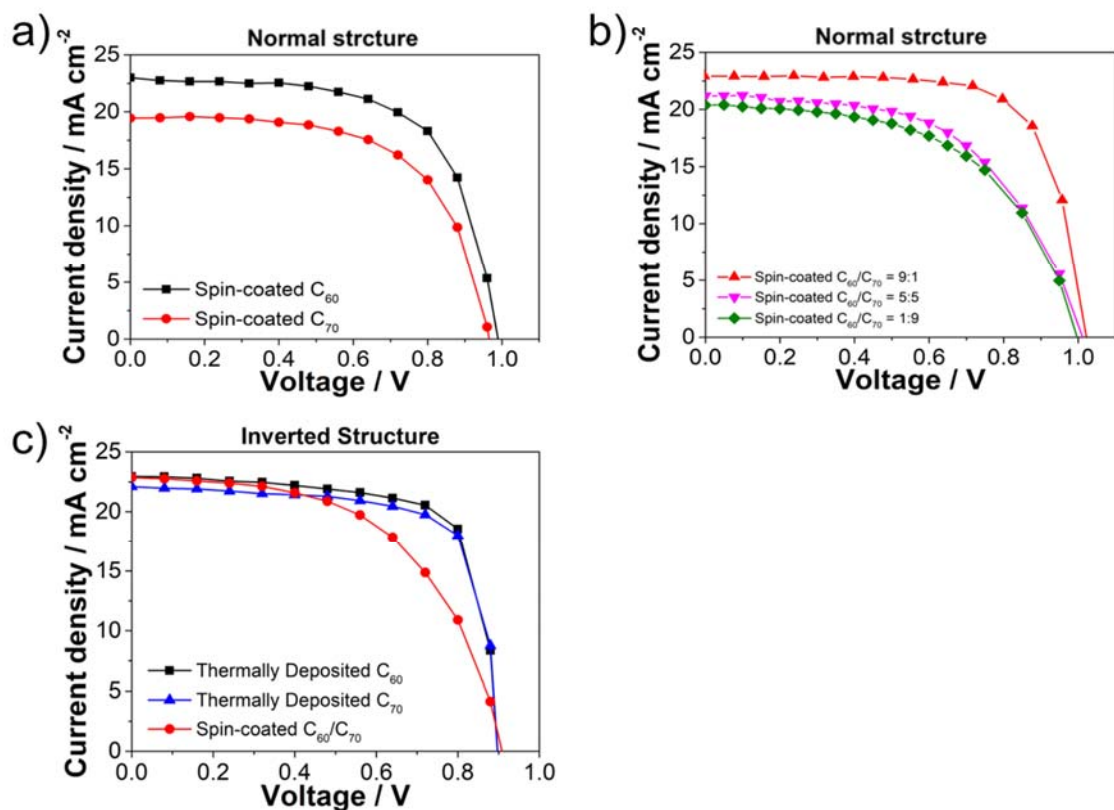
Figure S7. *J–V* curves of a) the normal-type PSCs using spin-coated C_{60}- (black) and C_{70}- (red); the normal-type PSCs using b) mixed fullerenes with different C_{60} to C_{70} ratios; c) the inverted-type PSCs using thermally deposited C_{60}- (black) and C_{70}- (red), and mixed fullerenes (blue).

Table S1. Photovoltaic parameters of the inverted-type PSCs using thermally deposited C_{60}, thermally deposited C_{70}, and spin-coated mix-fullerene as the ETLs under one sun (AM 1.5 G, 100 mW cm^{-2}).

Fullerene	J_{SC} [mA cm^{-2}]	V_{OC} [V]	FF	R_S [Ω cm^2]	R_{SH} [Ω cm^2]	PCE$_{Best}$	PCE$_{Average}$	Hysteresis Index
C_{60}	22.9	0.90	0.77	9	1.1×10^4	15.8%	15.3% ±0.4	0.01
C_{60}/C_{70}=9:1	22.1	0.90	0.76	10	1.0×10^4	15.2%	15.0% ±0.5	0.01
C_{70}	22.9	0.91	0.55	27	7.2×10^3	11.4%	11.3% ±0.3	0.02
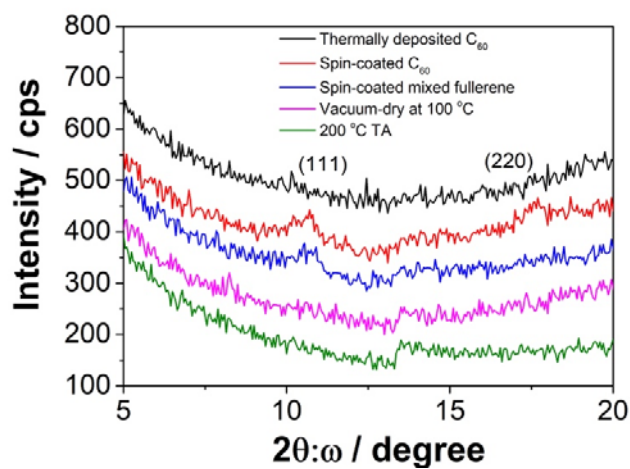
Figure S8. GIXRD scan of the thermally deposited C_{60} film (black), the spin-coated C_{60} film (red), the spin-coated mixed fullerene film (blue), the vacuum-dried mixed fullerene film (purple), and 200 °C TA-treated mixed fullerene film.
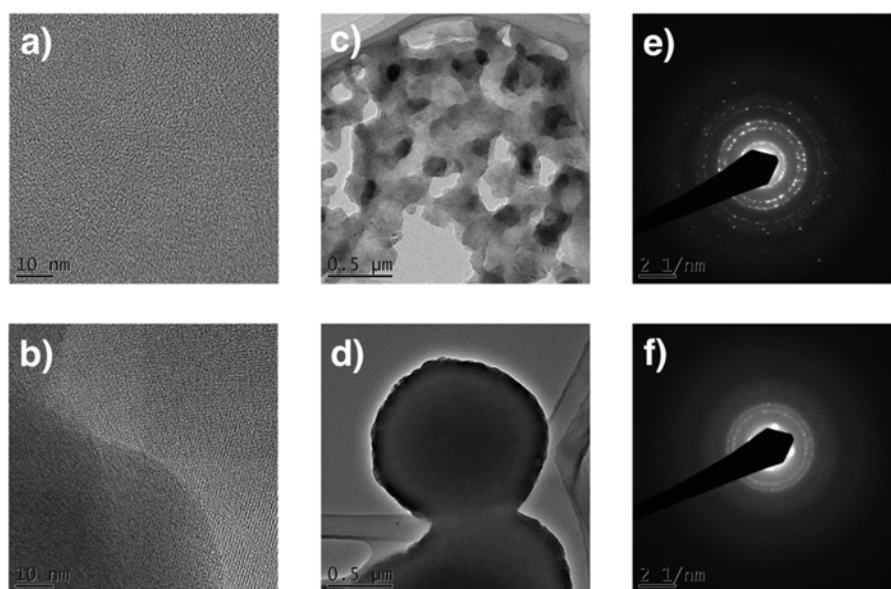

Figure S9. Supplementary TEM images of a) a thermally deposited C_{60} film, b) a boundary of crystal domains in a spin-coated C_{60} film, c) many crystal domains in a spin-coated C_{60} film, d) one large uniform domain in a mixed fullerene film, and supplementary SAED of d) a spin-coated C_{60} film and e) a mixed fullerene film.

Comparison of solids at the DFTB level (dispersion correction with the Grimme scheme):[S7]
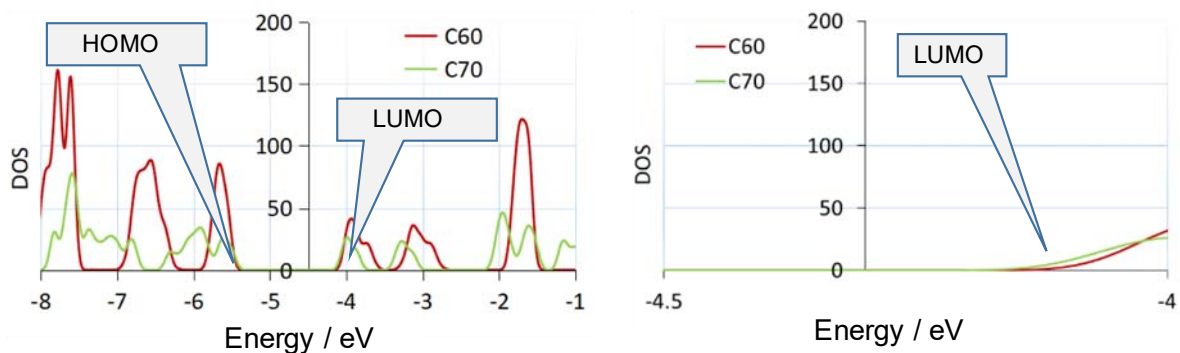
a) Density of states (DOS) of C_{60} and C_{70} crystals (left) with the LUMO magnified (right), showing the C_{60} and C_{70} LUMO position separately.
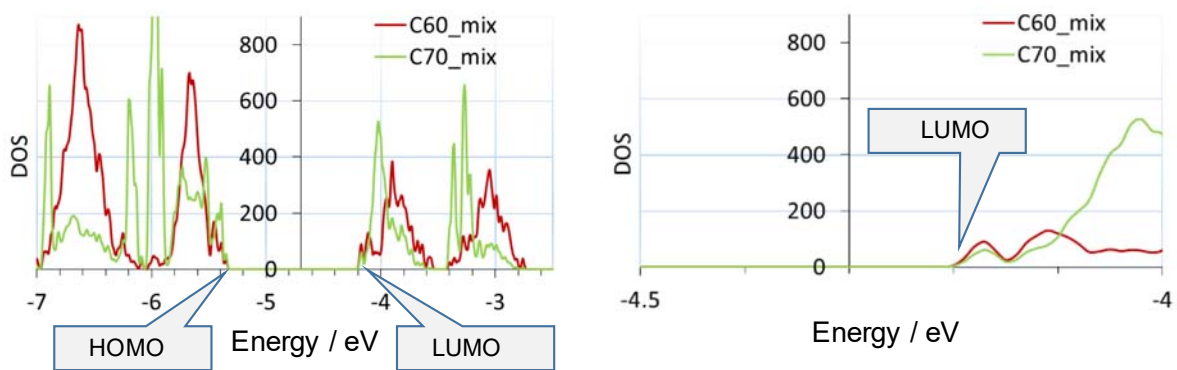
b) DOS of C_{60} and C_{70} parts in the mixed C_{60}/C_{70} structure.

Figure S10. Densities of states of a) C_{60} and C_{70}, and b) mixed fullerene (C_{60}:C_{70} 29:3) in solid state at the DFTB level.

Effect on surface on DOS at the DFTB level:

111 surface of C_{60} in fcc structure:

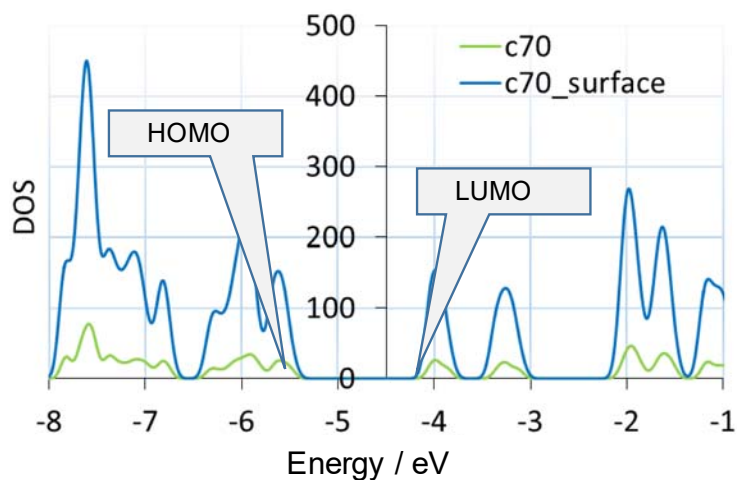DOS of C$_{60}$ and 111 surface of C$_{60}$:
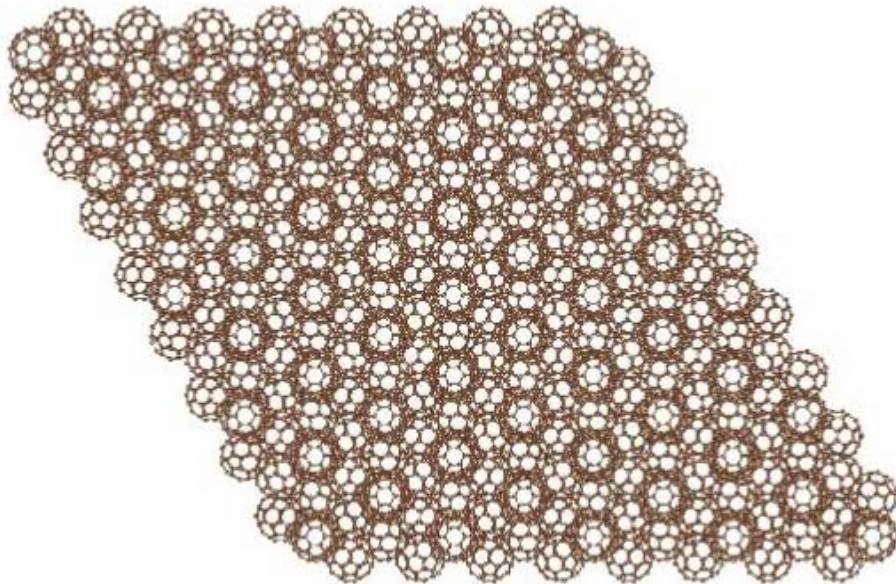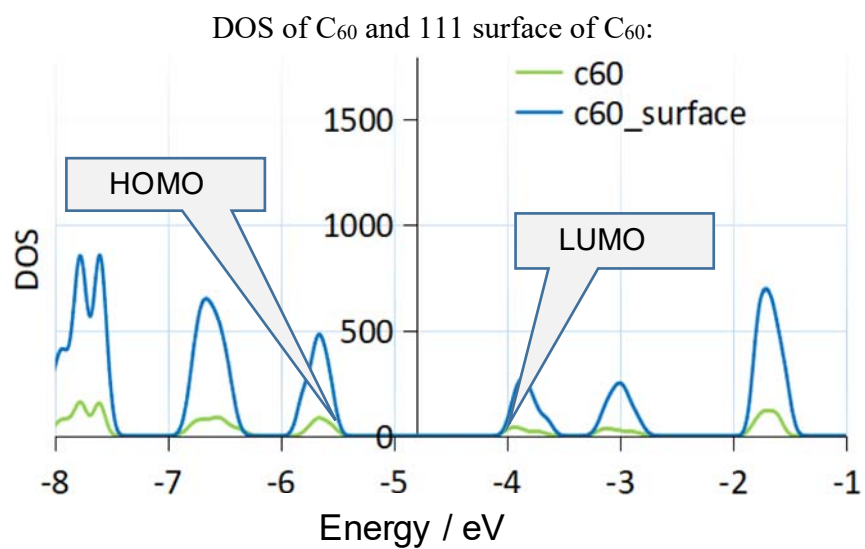
001 surface of C$_{70}$ in hcp structure:
Similar to C$_{60}$, we cut the 001 surface of C$_{70}$ hcp crystal.
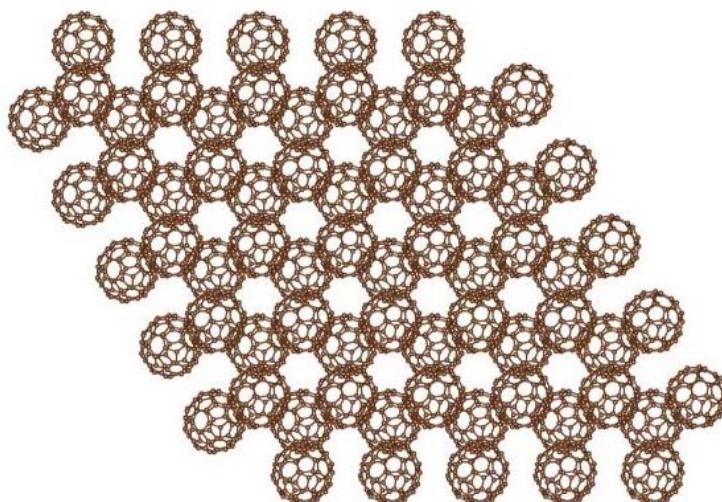
DOS of C$_{70}$ and 001 surface of C$_{70}$:

The lowest energy surfaces of both the C_{60} and C_{70} crystal behave similar with the bulk.

Figure S11. Computational energy level calculations of C_{60}, C_{70} , and mixed fullerene in which crystallinity and surface have been taken into account in solid at DFTB level.

Convex hull: It seems from the convex hull that there is very small possibility of segregation in mixed system, as the formation energy change is negligible (~0.03 eV, i.e on the order of kT). Thus, the mixed C_{60}/C_{70} system likely does not segregate into C_{60}/C_{70} layers.
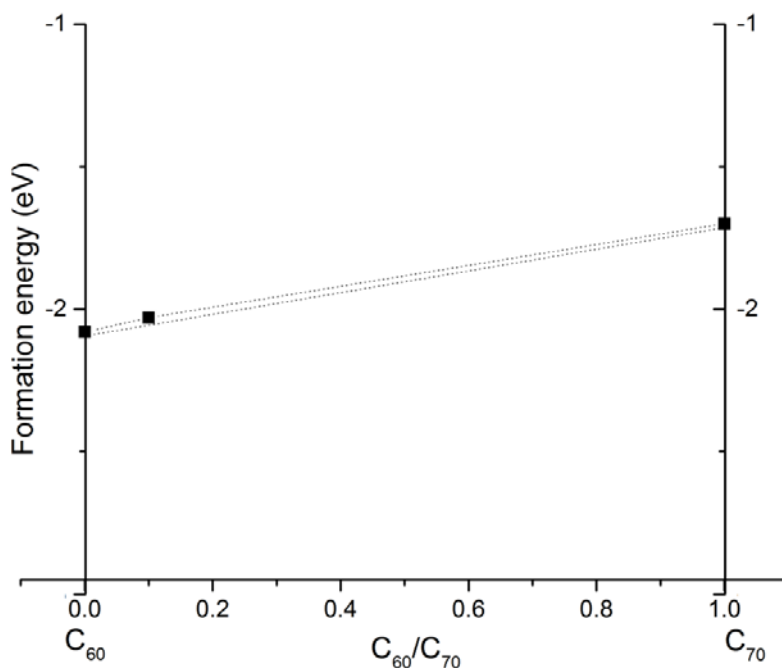
The electron transfer rate of C_{60}/C_{70} mixed system.

Figure S12. Segregation mechanism calculation of C_{60} and C_{70} mixture and electron transfer rate calculation.
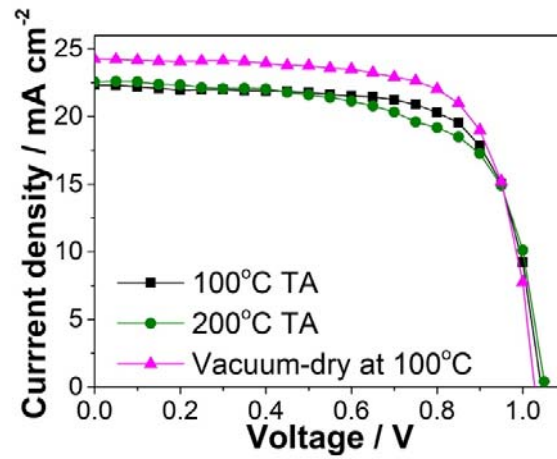

Figure S13. *J–V* curves of PSCs after 100 °C TA (green line), 200 °C TA (blue line), and 100 °C TA under light vacuum (purple line) on spin-coated mixed fullerene ETLs.
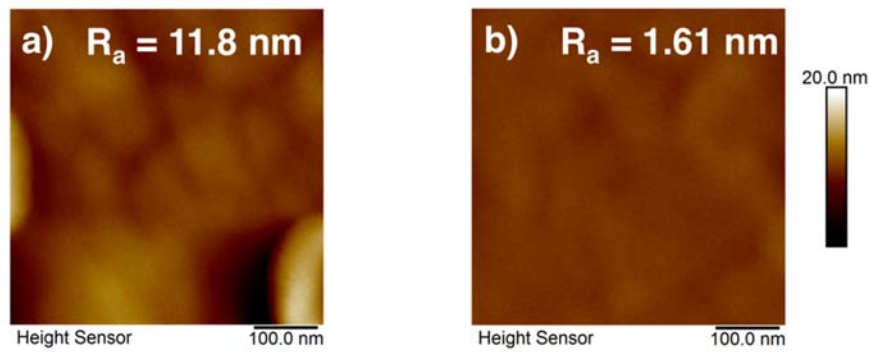

Figure S14. AFM images of a) 200 °C TA-treated spin-coated mixed fullerene film, and b) 100 °C TA-treated under light vacuum of spin-coated mixed fullerene film.
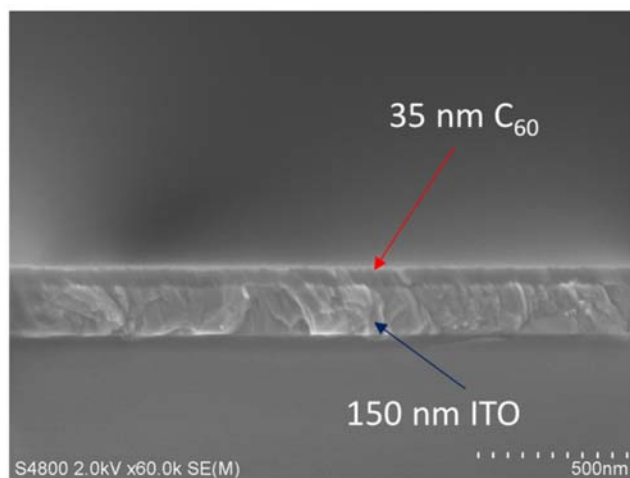
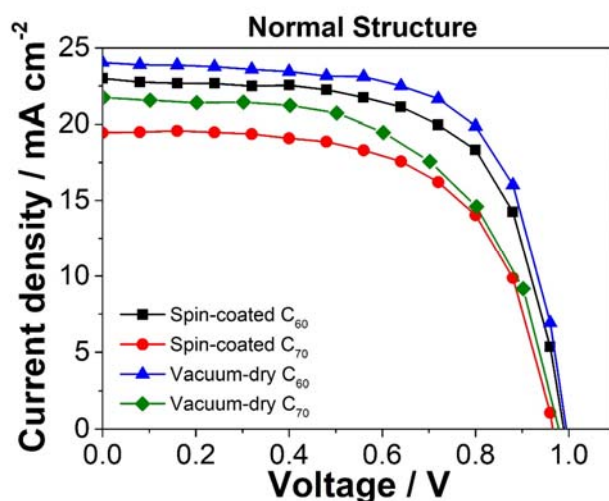**Figure S15**. Cross sectional SEM of thermally deposited C_{60} on ITO substrate.

Figure S16. *J–V* curves of the normal-type PSCs using spin-coated C_{60} (black), spin-coated C_{70} (red), vacuum-dry C_{60} (blue), and vacuum-dry C_{70} (green).

Table S2. Photovoltaic parameters of the normal-type PSCs using spin-coated C_{60}, C_{70} as the ETLs with vacuum-dry treatment under one sun (AM 1.5 G, 100 mW cm^{-2}).

Fullerene	J_{SC} [mA cm^{-2}]	V_{OC} [V]	FF	R_S [Ω cm^2]	R_{SH} [Ω cm^2]	PCE_{Best}	$PCE_{Average}$	Hysteresis Index
C_{60}	23.0	0.99	0.65	42	1.7×10^4	14.8%	14.6% ±0.7	0.03
Vacuum-dry C_{60}	24.1	0.99	0.67	37	1.0×10^4	16.0%	15.7% ±0.5	0.03
C_{70}	19.5	0.97	0.62	36	6.8×10^4	11.7%	11.4% ±0.6	0.07

Vacuum-dry C_{70}	21.7	0.98	0.60	38	1.2×10^4	12.1%	11.9% ±0.4	0.05

SUPPORTING REFERENCES

S1) Frisch, M. J.; Trucks, G. W.; Schlegel, H. B.; Scuseria, G. E.; Robb, M. A.; Cheeseman, J. R.; Scalmani, G.; Barone, V.; Mennucci, B.; Petersson, G. A.; Nakatsuji, H.; Caricato, M.; Li, X.; Hratchian, H. P.; Izmaylov, A. F.; Bloino, J.; Zheng, G.; Sonnenberg, J. L.; Hada, M.; Ehara, M.; Toyota, K.; Fukuda, R.; Hasegawa, J.; Ishida, M.; Nakajima, T.; Honda, Y.; Kitao, O.; Nakai, H.; Vreven, T.; Montgomery Jr., J. A.; Peralta, J. E.; Ogliaro, F.; Bearpark, M.; Heyd, J. J.; Brothers, E.; Kudin, K. N.; Staroverov, V. N.; Kobayashi, R.; Normand, J.; Raghavachari, K.; Rendell, A.; Burant, J. C.; Iyengar, S. S.; Tomasi, J.; Cossi, M.; Rega, N.; Millam, J. M.; Klene, M.; Knox, J. E.; Cross, J. B.; Bakken, V.; Adamo, C.; Jaramillo, J.; Gomperts, R.; Stratmann, R. E.; Yazyev, O.; Austin, A. J.; Cammi, R.; Pomelli, C.; Ochterski, J. W.; Martin, R. L.; Morokuma, K.; Zakrzewski, V. G.; Voth, G. A.; Salvador, P.; Dannenberg, J. J.; Dapprich, S.; Daniels, A. D.; Farkas, Ö.; Foresman, J. B.; Ortiz, J. V; Cioslowski, J.; Fox, D. J. Gaussian 09, Revision D.01. *Gaussian Inc.* **2009**, Wallingford CT.

S2) Becke, A. D. Density-functional thermochemistry. III. the role of exact exchange *J. Chem. Phys.* **1993**, *98*, 5648–5652.

S3) Perdew, J. P.; Burke, K.; Ernzerhof, M. Generalized gradient approximation made simple *Phys. Rev. Lett.* **1996**, *77*, 3865–3868.

S4) Aradi, B.; Hourahine, B.; Frauenheim, T. DFTB+, a sparse matrix-based implementation of the DFTB method *J. Phys. Chem. A* **2007**, *111*, 5678–5684.

S5) Lu, X.; Gaus, M.; Elstner, M.; Cui, Q. Parametrization of DFTB3/3OB for magnesium and zinc for chemical and biological applications *J. Phys. Chem. B* **2015**, *119*, 1062–1082.

S6) Kubillus, M.; Kubař, T.; Gaus, M.; Řezáč, J.; Elstner, M. Parameterization of the DFTB3 method for Br, Ca, Cl, F, I, K, and Na in organic and biological systems *J. Chem. Theory Comput.* **2015**, *11*, 332–342.

S7) Grimme, S. Semiempirical GGA-type density functional constructed with a long-range dispersion correction *J. Comput. Chem.* **2006**, *27*, 1787–1799.